Design of Multilayers of Urchin-like ZnO Nanowires Coated with TiO 2 Nanostructures for Dye-Sensitized Solar Cells

Chantal Karam, Roland Habchi, Sophie Tingry, Philippe Miele, Mikhael Bechelany

Design of Multilayers of Urchin-like ZnO Nanowires Coated with TiO_2 Nanostructures for Dye-Sensitized Solar Cells

Chantal Karam[a], Roland Habchi[b], Sophie Tingry[a], Philippe Miele,[a] Mikhael Bechelany[a]*

[a]Institut Européen des membranes, IEM, UMR-5635, Université de Montpellier, ENSCM, CNRS, Place Eugène Bataillon, 34095 Montpellier cedex 5, France

[b]EC2M, faculty of sciences 2, Campus Pierre Gemayel, Fanar, Lebanese University, 90656 Lebanon.

* Corresponding authors: mikhael.bechelany@umontpellier.fr, Phone: +33467149167, Fax: +33467149119

ABSTRACT

In dye-sensitized solar cells, the photovoltaic efficiency of nanowires (NW) is still limited by their surface area and loss of light absorption compared with nanoparticle (NP) architectures. To overcome this limitation, the light harvesting efficiencies must be improved by increasing the total NW array surface area, without increasing too much the traveled distance of electrons. Here, we describe the design of a 3D architecture based on polystyrene spheres (PS) coated with ordered multilayers of urchin-like ZnO NWs (U-ZnO NWs) to be used as a high surface area nanostructure photoanode for dye-sensitized solar cells. Two to four layers of U-ZnO NWs were synthesized by using PS of 1 and 5 µm in diameter. The ordered layers of U-ZnO NWs were

then coated with a thin layer of TiO_2 by atomic layer deposition, and topped with a ~ 9-14 µm thick layer of anatase TiO_2 NPs. We found that assembling organized layers of U-ZnO NWs significantly increased the surface area and provided better photon absorption. Moreover, coating the U-ZnO NWs with a thin TiO_2 layer decreased the charge recombination and consequently enhanced the photovoltaic efficiency.

Keywords: Dye sensitized solar cells, core-shell nanostructures, multilayers of urchin-like ZnO nanowires, TiO_2, Atomic Layer Deposition

INTRODUCTION

Nanostructured solar cells, such as dye-sensitized (DSSC), perovskite and organic solar cells, have been integrated in the photovoltaic field as an alternative to traditional solar cells owing to their low manufacturing cost and ease of fabrication [1, 2]. The principle behind a nanostructured solar cell consists of increasing the surface area of the photo-anode to improve light absorption and consequently the photogeneration of charges, and to improve the carrier transport on shorter transport distances. However, increasing the surface area of the photo-anode also increases the charge recombination rates at the numerous surfaces and interfaces. The introduction of thin recombination barrier layers at these interfaces can minimize this recombination [2], and a compromise has to be found between surface area, light absorption/photogeneration and recombination. For instance, in DSSCs (the most widely studied nanostructured solar cells during the last decades), the electrons generated upon solar light absorption by the dye molecules are injected into the conduction band of a wide gap semiconductor (*i.e.*, TiO_2, ZnO) and are finally collected by an electrode. Then, the redox couple of the electrolyte (*i.e.*, I/I^{3-}) can regenerate electrons at the dye molecules [3]. DSSCs are typically composed of zero-D

nanostructures based on crystalline mesoporous nanoparticles (NPs) of titanium oxide (TiO_2). However, the morphology of TiO_2 NPs hampers electron transport [4, 5]. Indeed, the large surface area of the mesoporous film promotes the adsorption of dye molecules on TiO_2 NPs [5]; however, the high density of grain boundaries significantly increases the recombination of electron-hole pairs and subsequently reduce the overall photovoltaic efficiency, despite this large surface area [5]. The development of 1D nanostructures based on conducting scaffolds (i.e., indium tin oxide nanowires [6]) or semiconductor nanowires/nanotubes (i.e., ZnO, TiO_2 [7]) has reduced the charge recombination problem and the electron transport distance for collection [8-11], leading to an increment of the electron collection efficiency [12-14].

Although nanowires (NWs) provide direct electrical pathways that facilitate the carrier collection, their photovoltaic efficiency is still limited by their surface area [15-17] and loss of light absorption [13] compared with NP architectures. To overcome this limitation, the light harvesting efficiencies must be improved by increasing the total NW array surface area by precisely controlling the dimensions of each NW [15-17]. To address this issue, we previously developed a new architecture of well-organized urchin-like single-crystal ZnO NWs (U-ZnO NWs) with controlled NW dimensions for photovoltaic applications [13, 18, 19]. For its synthesis, we employed surface structuring methods (self-assembling of polystyrene spheres, PS), followed by atomic layer deposition (ALD) and electrodeposition (ECD) of layers of ZnO NWs. ALD is a cost-efficient method that could be used to grow ultra-thin and uniform layers at an industrial level [20]. ECD of ZnO NWs in solution is a low-energy (temperature <100°C) technology that is well suited for large-scale production at lower cost compared with chemical vapor deposition, molecular beam epitaxy and physical vapor deposition [21-25]. Our synthesis method gives a 3D architecture with a precise control of the NW dimensions [19]. Indeed, by tuning the growth

parameters during ALD and/or ECD, or by modifying the PS diameter, it is possible to adjust the ZnO NW diameter, density and morphology [19]. The higher surface area of U-ZnO NWs (compared with ZnO NWs) and direct electron transport (owing to the lower amount of grain boundaries compared with commercial TiO_2) reduce the charge recombination and increase the collection efficiency [13, 14]. In addition, the unique geometry of U-ZnO NWs improves the optical absorption and light trapping through a wide range of wavelengths, while reducing optical reflection [19]. In our previous work, we found that deposition of a TiO_2 layer by ALD was necessary to make a working cell, and 10 nm of TiO_2 appeared to be the optimal thickness [19]. Here, we wanted to better understand the role of the photo-anode surface area and light scattering properties to improve the overall photovoltaic efficiency of our architecture. To this aim, we increased the surface area by adding multiple layers (2, 3 and 4) of U-ZnO NWs, and then coated the arrays of U-ZnO NW building blocks with a 10 nm-thick layer of TiO_2 by ALD to reduce the recombination of electron-hole pairs due to the increased surface area. Then, we infiltrated TiO_2 NPs as a mean to increase the photogeneration of charges in order to observe the effect of the different number of U-ZnO NW layers on the conversion efficiency.

MATERIALS AND METHODS

1. Deposition of polystyrene microspheres

PS spheres (diameter of ~ 5 µm and ~ 1 µm) in suspension (4 wt % aqueous dispersion; Thermo Fisher, USA) were deposited on transparent indium tin oxide (ITO)-coated glass (size 1 x 4 cm^2) (Kintec Company, Hong Kong) using the dip coating technique, as previously

described [19]. Prior to deposition of PS onto the ITO-coated glass, the substrate was cleaned carefully to remove the surface impurities. Two, three and four layers of PS spheres of 5µm in diameter (5µm-PS) were deposited on the ITO-coated glass, and after deposition of each layer, the sample was heated in a furnace at 100 °C for 30min to ensure the sphere adherence to the surface. The resulting multilayers of PS were exposed to oxygen plasma to reduce their size. The pressure was fixed at 0.7 mbar and the power supply at 0.2 A. The appropriate plasma exposure time, to precisely control the PS size, depends on their initial size [5]. For 5µm-PS, the optimal plasma exposure time was 25 min.

PS spheres of 1µm in diameter (1µm-PS) were also deposited on the ITO-coated glass. 200 µL of a carboxylate modified 1µm-PS suspension was diluted with equal amount of ethanol. 40 µL of the resulting solution was deposited on a clean glass substrate (size 2 x 2 cm^2) previously treated with oxygen plasma for 2 min to render the surface more hydrophilic. The glass substrate was then immersed in a dish (size 5 x 5 cm^2) filled with distilled water and fixed at an angle of 45°. The same process was repeated to obtain PS multilayers. The same oxygen plasma conditions were used to reduce the sphere size with an exposure time of 5 min.

2. Synthesis of ZnO urchins

An ultrathin and uniform ZnO film was homogeneously deposited on the ITO-coated glass covered with multilayers of PS using a custom-made ALD reactor at low temperature [28-31]. ALD is a high quality method for vapor deposition of ultra-thin homogeneous layers that permits to precisely control the layer thickness down to the angstrom range at relatively low temperatures [26, 27]. The ZnO layer i) fixes the multilayers of PS on the substrate; ii) generates an electroactive surface to make a conductive electrode for electrodeposition; iii) acts as a seed layer for the ZnO

NW growth; and iv) plays a role in the hole blocking barrier to avoid short circuits between the substrate and the p-type material [18].

Deposition of the ZnO seed layer by ALD requires the use of diethylzinc (DEZ, $(Zn(CH_2CH_3))_2$, 95% purity, Sigma Aldrich)), as zinc precursor, and water (H_2O). Sequential DEZ and H_2O exposures, separated by Argon purge, were applied, as previously described [18]. 20nm-thick layers of ZnO deposited on the ITO/glass coated with PS multilayers were synthesized by applying 100 ALD cycles at the temperature of 80°C ($ITO/PS_{multilayers}/ZnO_{ALD}$). ZnO NWs were then electrodeposited on the $ITO/PS_{multilayers}/ZnO_{ALD}$ (ECD process) using a three-electrode electrochemical cell (platinum wire as the counter electrode, an Ag/AgCl electrode as the reference electrode, and ZnO NWs as the working electrode) containing an aqueous solution of zinc chloride (5.10^{-4} M) and potassium chloride (0.1M) as salt. Prior to the growth process, the aqueous solution was saturated with molecular O_2, and the ECD (80°C for 4 hours) was carried out using an Autolab VersaSTAT3 potentiostat at the potential of -1 V vs Ag/AgCl. After the ECD, the PSs were removed by annealing the samples in air at 450 °C for 1h to improve the ZnO NW crystallinity. These steps define the organized multilayers of U-ZnO NWs.

3. Atomic layer deposition of TiO_2 and dye-sensitized solar cell fabrication

First, conformal 9nm thick films of TiO_2 were deposited on the multilayers of U-ZnO NWs using the ALD reactor to generate the core-shell structure and to form the recombination barrier layers. The deposition of the TiO_2 shells was performed by sequential exposures to Titanium Tetra-Isopropoxide (TTIP) heated to 90 °C and H_2O heated to 40 °C in the ALD reactor at 60 °C. The TiO_2 deposition cycle consisted of a TTIP pulse for 5s followed by exposure for 10s and purge for 60s, and then of a H_2O pulse for 2s with 10s exposure and 60s purge (160 cycles to obtain 9 nm-thick shells of TiO_2).

Then, a mesoporous film of anatase TiO_2 NPs (P25 Solaronix) was deposited on top of the ZnO/TiO_2 core-shell structures by drop-casting. First, 0.77g of anatase TiO_2 NPs (diameter ~ 20 nm, 0.077 wt % aqueous dispersion) was diluted in 12.5 mL of absolute ethanol (99.8%) and immersed in an ultrasonic bath for ~ 40min. The thickness of the anatase TiO_2 NPs deposited on top of the ZnO/TiO_2 core-shell was optimized to completely coat the multilayers of U-ZnO NWs. It was determined that five drops corresponded to ~ 1µm-thick layer of TiO_2 NPs. After the deposition of TiO_2 NPs, 1nm-thick layer of TiO_2 was deposited by ALD for surface passivation.

Samples were annealed in air at 450 °C for 30min, and then immersed in a solution of Ru dye 20 mg (N719, Solaronix) diluted in 50 mL of methanol for 12h. For DSSC fabrication, the films were rinsed in ethanol, dried, and then assembled to a platinum counter-electrode separated by a 60µm-thick hot-melt film (Solaronix). The DSSC internal space was filled with an iodide electrolyte (AN-50, Solaronix). Cells were immediately illuminated by 500 Wm^{-2} simulated sunlight through a black cover with an aperture of 0.7 x 0.7 cm^2, 0.8 x 0.7 cm, or 0.9 x 0.7 cm, in function of the sample size.

4. Characterization

A Scanning Electron Microscope (SEM, Hitachi S-4800) was used to observe the sample morphology. X-ray diffraction analysis on a Bruker D-8 GADDS diffractometer (Co Kα) allowed determining the sample crystalline structure and orientation. Ultra-fine characterization by High-Resolution Transmission Electron Microscope (HRTEM, JEOL ARM 200F Cold-FEG) allowed determining the U-ZnO NW crystalline quality and orientation. A Focused Ion Beam system (FIB, ZEISS NVISION 40 FIB/SEM) was used to determine many fundamental parameters, such as the NW length, radius and density per urchin, number of urchins per unit surface, and urchin dimensions.

The reflectivity and transmission of the ZnO/TiO_2 core-shell nanostructure building blocks were characterized with a spectrophotometer (Lambda 900, Perkin Elmer). DSSC current–voltage (J–V) measurements were carried out under full simulated sunlight illumination (500 $W.m^{-2}$). A photodetector was used to measure the voltage per W/m^2 at a specific distance to obtain 500 $mWcm^{-2}$ as incident irradiance. It's noteworthy that an important photoconversion efficiency (PCE) variations are observed when using irradiance lower than 500 $mWcm^{-2}$ [32]. Samples were illuminated from the ITO-coated glass side. The characteristic parameters of the solar cells, including the short-circuit current density (J_{sc}), open-circuit voltage (V_{oc}), fill factor (FF) and PCE, were extracted from the J–V curves.

RESULTS

1. Synthesis and characterization of the multilayers of U-ZnO NWs (with PS of ~ 5 µm and ~ 1 µm in diameter)

First, PS of two different diameters (5 µm and ~ 1 µm) were coated with ordered multilayers of U-ZnO NWs, and the structural features of the samples were characterized in function of the number of urchin layers.

1.1. Structural characterization of U-ZnO NWs

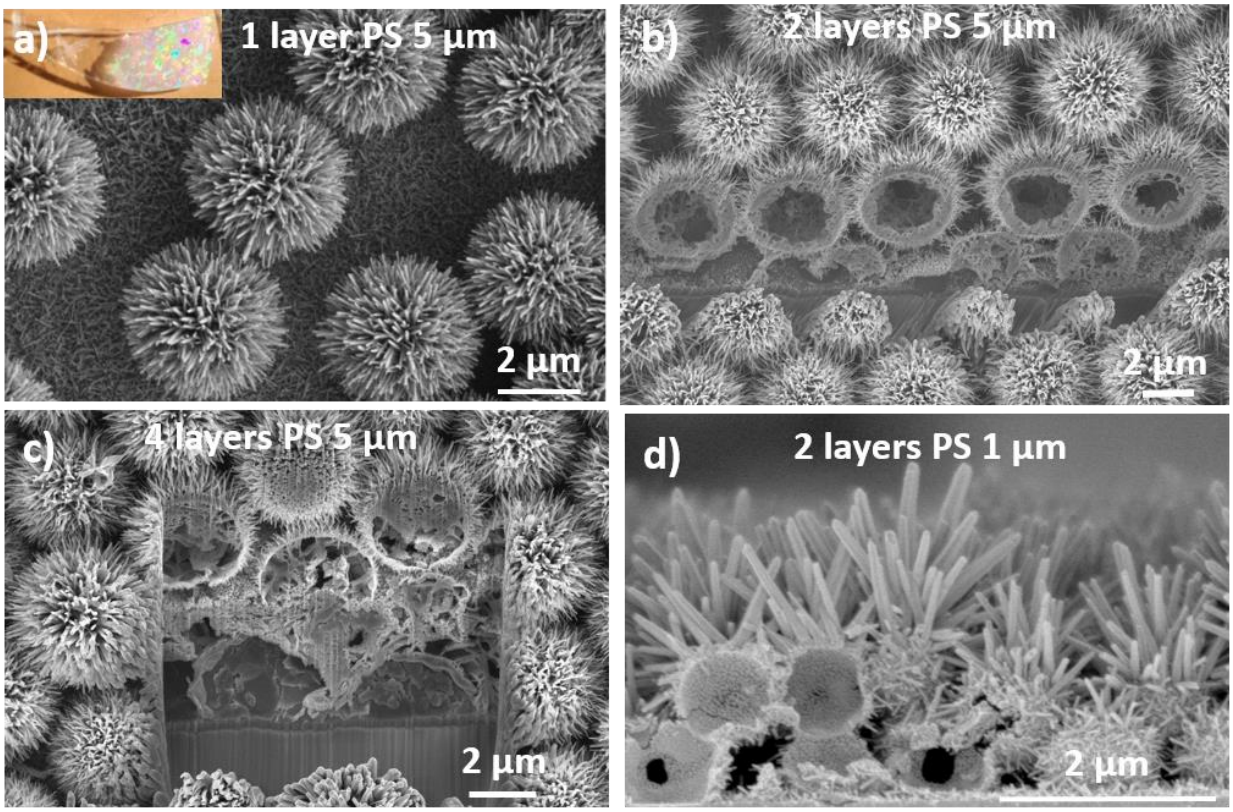

Figure 1. SEM images of the multilayers of U-ZnO NWs: (a) top view of a monolayer of U-ZnO NWs (PS ~ 5 µm in diameter). The inset shows a macroscopic view of the sample. (b) Cross-sectional image of two layers of U-ZnO NWs (PS ~ 5 µm in diameter) after FIB milling. The ZnO NWs are ~ 948 nm long and have a diameter of ~ 57 nm. (c) Longitudinal cross-sections of U-ZnO NWs (PS ~ 5 µm in diameter) after FIB milling showing the four regularly arranged layers of U-ZnO NWs. (d) Longitudinal cross-sections of U-ZnO NWs (PS ~ 1 µm in diameter) after FIB milling showing two regularly arranged layers of U-ZnO NWs.

SEM analysis indicated that the resulting ordered multilayers of U-ZnO NWs (5µm- and 1µm-PS) were deposited on the entire sample surface (Figure S1a and S1d, respectively; see Supporting Information), and that this deposition was uniform over a large sample area (inset of Figure 1a shows a macroscopic view of the sample). The U-ZnO NW multilayers displayed a

good adherence to the ITO-coated glass substrate due to the ZnO ALD layer that fixes the PS to the substrate. This is further supported by their ability to transport electrons to the ITO as demonstrated in our previous work [19].

The ZnO NW crystal quality was confirmed by TEM (Figure 2). These NWs grown using ECD are known to have a layer by layer growth mechanism with alternate layers of positive Zn ions and negative O ions due to polarity effects [33]. The fast-Fourier transform (Figure 2) and other selected area electronic diffraction (SAED) patterns taken from several ZnO NW zones indicated that the ZnO NWs were single crystals and the growth was along the preferential orientation [0001]. The resolved lattice fringes along the c-axial growth direction measured 5.2 Å, which is in agreement with the (0001) plane of the hexagonal ZnO crystal structure. The X-ray diffraction spectra of the multilayered U-ZnO NWs showed the characteristic peaks of the ZnO wurtzite structure with the main orientations of (100) at 34.4°, (002) at 35.2°, and (101) at 36.3° (Figure S3, Supporting Information).

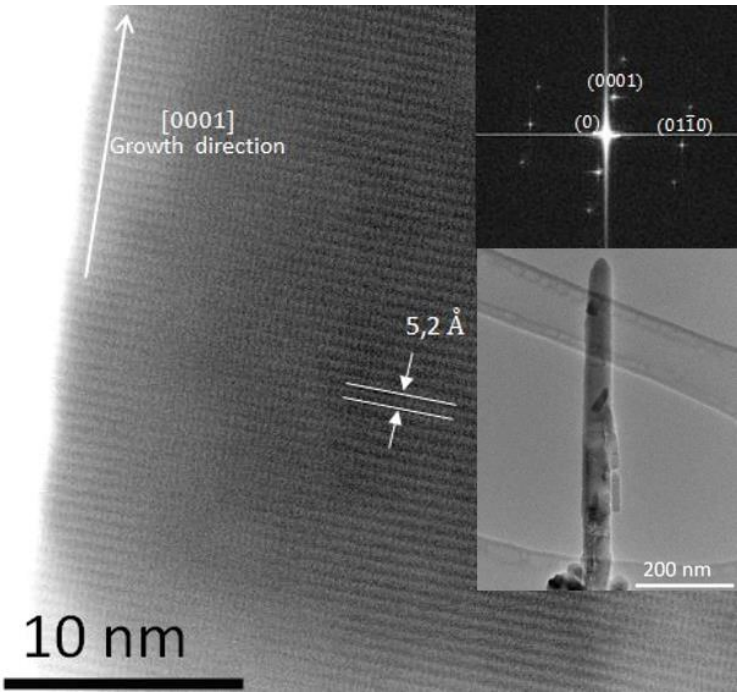

Figure 2. HRTEM image showing the high crystalline quality of as-grown ZnO NWs. The Fast-Fourier Transform (FFT) indicates that the preferential orientation is [0001] and that the distance between the atomic planes in this direction is 5.2 Å. The inset shows a low-resolution TEM image of the entire nanowire.

As mentioned previously, the NW diameter, density and morphology can be controlled by finely regulating the growth parameters during the deposition process, and therefore the approximate number of NWs and surface area could be calculated for different (1 to 4 layers) of U-ZnO NWs (Table 1). For the multilayers of U-ZnO NWs (~ 5µm-PS), etching using oxygen plasma for 25min decreased the PS size from 5 µm to 4 µm, thus leaving 1 µm spacing between PS spheres (Figure S2a, Supporting Information). For the multilayers of U-ZnO NWs (~ 1µm-PS), etching was performed for 5min, leaving 0.5 µm spacing between PS spheres (Figure S2b, Supporting Information). For a 20nm-thick ZnO ALD layer, the length of the ZnO NWs was ~ 950 nm, with a mean diameter of ~ 57 nm. The density of ZnO NWs (~ 5µm-PS) was ~ 5260 NWs/urchin [19].

As the urchin density was ~ 4.7 million urchin/cm^2, this gave ~ 25 billion NWs/cm^2 (Table 1). Conversely, the density of ZnO NWs (~ 1µm-PS) was lower (302.96 NWs/urchin compared with 5260 NWs/urchin for ZnO NWs with ~ 5µm-PS). However, the number of urchins per unit surface for the microstructures with 1µm-PS was higher (156.25 million urchin/cm^2 vs 4.7 million urchin/cm^2 for 5-µm PS) because of their smaller size. Consequently, the NW number per unit surface was higher for 1µm-PS (~ 47 billion NWs/cm^2) (Table 1).

The number of NWs/cm^2 was increased by adding more urchin layers (for both PS diameters). Indeed, by adding 1, 2 or 3 more layers, the number of NWs/cm^2 increased proportionally. Then, the overall active surface area of the U-ZnO per unit surface, which is the substrate surface area, was ~ 42.25 cm^2 (5µm-PS) and ~ 80.2 cm^2 (1µm-PS). The ZnO NW density and overall active surface area values function of the layer number and PS diameter are presented in Table 1.

Table 1. Density and total active surface area of U-ZnO NWs in function of the number of layers and PS diameter (5 and 1 µm).

Samples (U-ZnO NWs)	**Density of ZnO NWs (10^9 x cm^{-2})**		**Active surface area (cm^2)**	
	PS ~ 5 µm	**PS ~ 1 µm**	**PS ~ 5 µm**	**PS ~ 1 µm**
1 layer	~25	~47	~42	~80
2 layers	~50	~94	~84	~160

3 layers	~75	~141	~126	~240
4 layers	~100	~188	~169	~320

1.2. Optical characterization of U-ZnO NWs

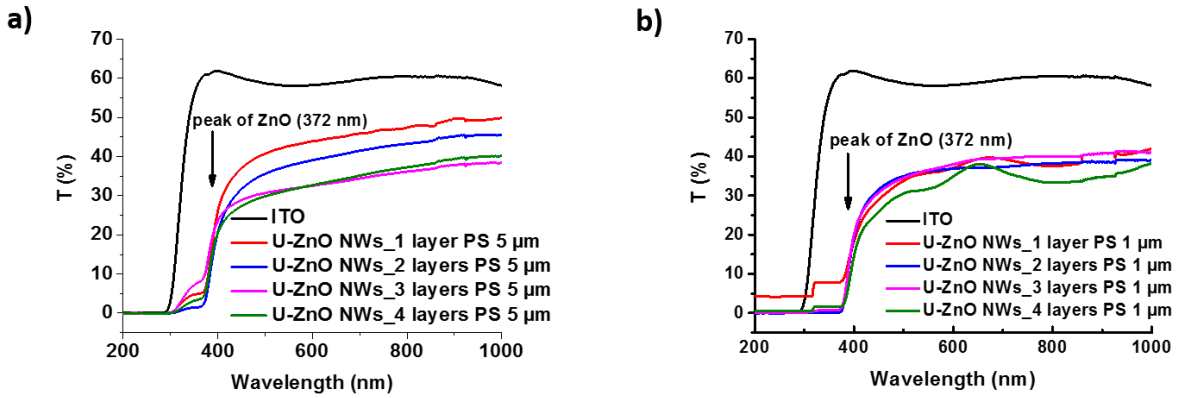

Figure 3. Transmittance spectra of multilayer U-ZnO NWs in function of the PS diameter: **a)** ~ 5 µm and **b)** ~ 1 µm.

Then, the spectral dependence of transmittance was assessed in function of the number of U-ZnO NW layers and the PS diameter (5 µm and 1 µm) to determine the influence of multilayer U-ZnO NWs on light scattering (Figure 3a and b). As the PS spheres were removed by annealing at high temperature after U-ZnO NW synthesis, they could not affect scattering. A UV transmittance edge close to 372 nm (3.3 eV) was detected for all analyzed U-ZnO NWs samples, which corresponds to the band gap of ZnO. Transmittance clearly decreased when the number of U-ZnO layers increased (samples with 5µm-PS) (Figure 3a). This effect was not so evident for samples based on 1µm-PS; the lower transmittance values for the U-ZnO NWs with 1µm-PS are

explained by the higher number of NWs compared with samples based on 5µm-PS (Table 1). Analysis of the spectral dependence of optical absorbance in multilayer U-ZnO NWs (Figure S4, Supporting Information) showed that for 5µm-PS samples, adding new layers of PS spheres increase the absorbance from 52% to 62%, due to the increase of matter in the sample. For 1µm-PS samples, the curves were harder to interpret, possibly because the PS did not cover the entire surface homogeneously. Finally, evaluation of the spectral dependence of optical reflection in multilayer U-ZnO NWs (Figure S5, Supporting Information) indicated that optical reflection remains stable at 1.5% in 1µm-PS samples (Figure S5b). Conversely, it slightly increased from 1% to 8% for 5µm-PS samples (Figure S5a) upon addition of new PS layers. Thus, the incident light was almost entirely absorbed by the multilayers of urchins, stressing the strong advantage of using high-surface area multilayer U-ZnO NWs to enhance light absorption.

2. Multilayers of core-shell ZnO/TiO_2 urchins and hybrid structure of nanoparticles.

In the second step, core-shell nanostructures were synthesized by covering the ordered multilayers of U-ZnO NWs with a 10 nm-thick amorphous layer of TiO_2 by ALD (at 60 °C with a growth rate of ~ 0.05 nm/cycle, as measured on Si substrates). It has been reported that this thickness is optimal for acting as a recombination barrier layer [19]. Finally, a mesoporous film of anatase TiO_2 NPs was deposited on top of the 10nm-thick ZnO/TiO_2 layer core-shell to increase the charge photogeneration. As amorphous TiO_2 has better wettability than anatase TiO_2, the infiltration of TiO_2 NPs was done before annealing. Then, samples were heated at 450 °C in air for 30min to obtain the anatase phase on the 10 nm thick TiO_2 film, as reported previously [19], to evaporate solvent residuals and to provide better contact between NPs. The introduction of TiO_2 NPs increases the surface area, and also the charge recombination [19]. The morphology of the

final material (U-ZnO NWs/$TiO_{2\ 10nm}$/$TiO_{2\ NPs}$) (Figure 4a), and the infiltration of the mesoporous TiO_2 NP film between urchins (Figure 4b) were assessed by SEM. Figure S6 shows the evolution of the structure coverage with TiO_2 NPs as a function of the number of drops deposited on the surface of the bilayers of U-ZnO NWs /$TiO_{2\ 10\ nm\ layer}$ sample. The core-shell nanostructure was entirely covered with 30 drops of TiO_2 NP (Figure S6c).

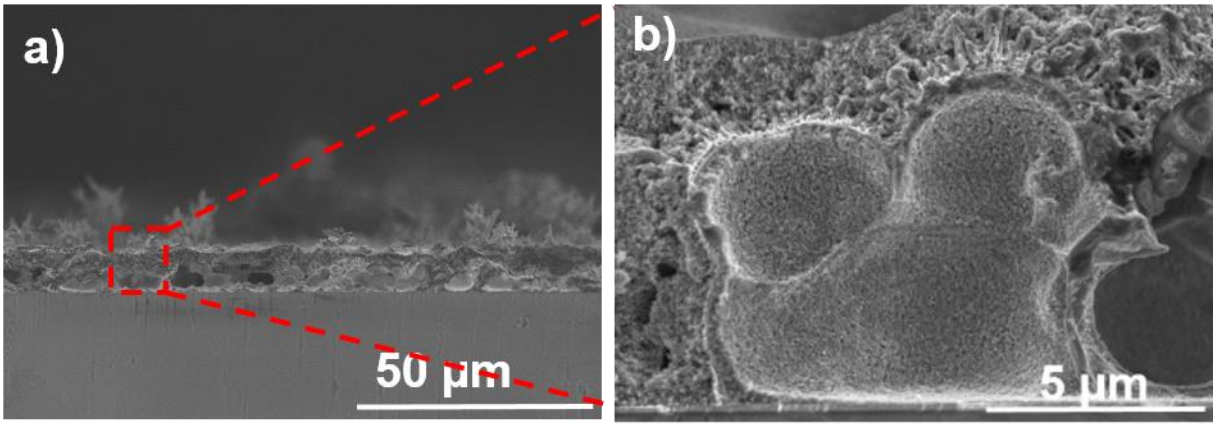

Figure 4. SEM images showing (a) a bilayer U-ZnO-NWs/TiO_2 core-shell coated with 10 nm of anatase TiO_2 and TiO_2 NP material, (b) the infiltration of the mesoporous TiO_2 NP film between urchins at higher magnification.

The thickness of the TiO_2 NP upper layer was increased proportionally to the number of U-ZnO NW layers and the PS diameter (Table 2). The optimal thickness of the TiO_2 NP layer was 9 -14 µm to cover entirely the multilayers prepared from 5µm-PS, and 2-4 µm for multilayers with 1µm-PS. This core-shell ZnO/TiO_2 urchin is a hybrid structure where the U-ZnO NWs play the role of a conductive scaffold, because the majority of the current will be transported through the urchin multilayers. For this reason, the main idea was to ensure the infiltration of the mesoporous TiO_2 NPs between urchins. We think that this process enhances the contact between NWs and

NPs, and decreases the distance of the electrons to be transported from the TiO_2 NPs to the U-ZnO NWs.

The surface area of commercial TiO_2 NPs is about 100 m^2/g with a size of 20 nm. A previous study [34] showed that the Ru dye diffuses through the mesoporous film of TiO_2 NPs. Therefore, increasing the active surface area should increase the amount of dye loading in our system, and consequently increase the photon absorption. Hence, it was important to assess the variation of the active surface area in function of the number of layers and the PS diameter. The active surface area for U-ZnO $_{NWs}$/$TiO_{2\ 10nm}$/$TiO_{2\ NP}$ core-shell structure depends on the number of U-ZnO NWs layers (Table 2, and calculations in Supporting Information), and it increases upon addition of TiO_2 NPs.

Table 2. Active surface area of U-ZnO NWs /$TiO_{2\ 10nm}$/$TiO_{2\ NPs}$ in function of the number of urchin layers and PS diameter.

Samples (U-ZnO$_{NWs}$/TiO$_{2\ 10nm}$/TiO$_{2\ NPs}$)		**TiO$_2$ NP thickness (µm)**		**TiO$_2$ NPs active surface area (µm^2)**		**Total active surface area (S $_{TiO2\ NPs}$ + S $_{U-ZnO\ NWs}$) (cm^2)**	
Number of U-ZnO NW layers	**Gasket dimensions (cm^2)**	**5µm-PS**	**1µm-PS**	**5µm-PS**	**1µm-PS**	**5µm-PS**	**1µm-PS**

1	0.7×0.7	6	2	43.3×10^9	-	453.6	-
	0.7×0.9	6	2	-	17.6×10^9	-	226
2	0.7×0.9	9	2	73.6×10^9	10.1×10^9	788.9	201
3	0.7×0.7	11	3	-	12×10^9	-	237.6
	0.7×0.9	11	3	79.1×10^9	-	870.3	-
4	0.7×0.8	14	4	86.2×10^9	18.1×10^9	956.6	360

The optical reflection of the U-ZnO NWs/$TiO_{2\ 10nm}$/$TiO_{2\ NPs}$ cell was analyzed (Figure S8a for 5µm-PS, and Figure S8b for 1µm-PS samples) after dye loading and illumination. For both PS sizes (1 µm and 5 µm), optical reflectance decreased in a broader range of wavelengths [200 nm – 550 nm] compared with U-ZnO NWs alone [200 nm – 380 nm], then increased exponentially, from 550 nm to 650 nm. This broader absorption is due to the presence of dye molecules and TiO_2 NPs in the system. As we were interested in the light harvesting process, the most interesting region in the spectra was located between 200 nm and ~ 550 nm (where our DSSCs absorb). However, for this wavelength interval, the reflectance spectra of 5µm-PS and 1µm-PS samples (Figure S8) were comparable, despite the small bumps (ups-and-downs that are in the range of 2% to 3%). In conclusion, all samples showed low reflectance; the highest variation recorded was ~ 3%, with no big difference when changing the number of layers. As different number of layers (for both PS sizes) influence the optical properties, we decided to focus on the transmission and absorption spectra that show variations upon changing the number of layers (see below).

The sample transmittance was tested before and after TiO_2 deposition to analyze the influence of the TiO_2 nanostructure on the transmittance of multilayer U-ZnO NWs. The transmittance of the U-ZnO NWs/$TiO_{2\ 10nm}$/$TiO_{2\ NPs}$ cell was evaluated function of the different number of urchin layers, before (Figure 5a, b) and after dye loading and illumination (Figure 5c, d) to determine the spectral influence. Before dye loading and illumination, the transmittance decreased from 51% to 35% upon deposition of four layers of U-ZnO NWs (with 5µm-PS) compared with a monolayer. This indicates the importance of using multilayers to enhance light absorption (Figure 5a). The mesoporous TiO_2 NPs film also contributed to reduce transmittance. Indeed, the thickness of the TiO_2 NP film increased from 6 µm for a monolayer to 14 µm for four layers of U-ZnO NWs (~ 5µm-PS) (Figure 5a). Thereby, by combining multilayers of ZnO urchins and a thick mesoporous layer of TiO_2 NPs, the surface area and dye loading should be further improved and consequently also the DSSC conversion efficiency. This hypothesis will be tested when studying the sample J-V curves.

For the 1µm-PS samples (Figure 5b), the transmittance variation was almost the same as for the 5µm-PS samples. However, as previously noted, the curves were harder to interpret due to some plain regions in these samples. Moreover, for four layers of U-ZnO NWs (1µm-PS), transmittance was almost 30% compared with 50% for the two-layer sample, indicating that the number of layers has an important effect on the optical transmission.

After dye loading and illumination, the spectral dependence of transmittance showed a broadening in the wavelength range in the presence of TiO_2 NPs on top of the U-ZnO NWs/$TiO_{2\ 10µm}$ layer (Figure 5c and d). This was due to the thick layer of TiO_2 NPs (10 µm) (Figure 5c and d) that increases the amount of dye loading [19, 35].

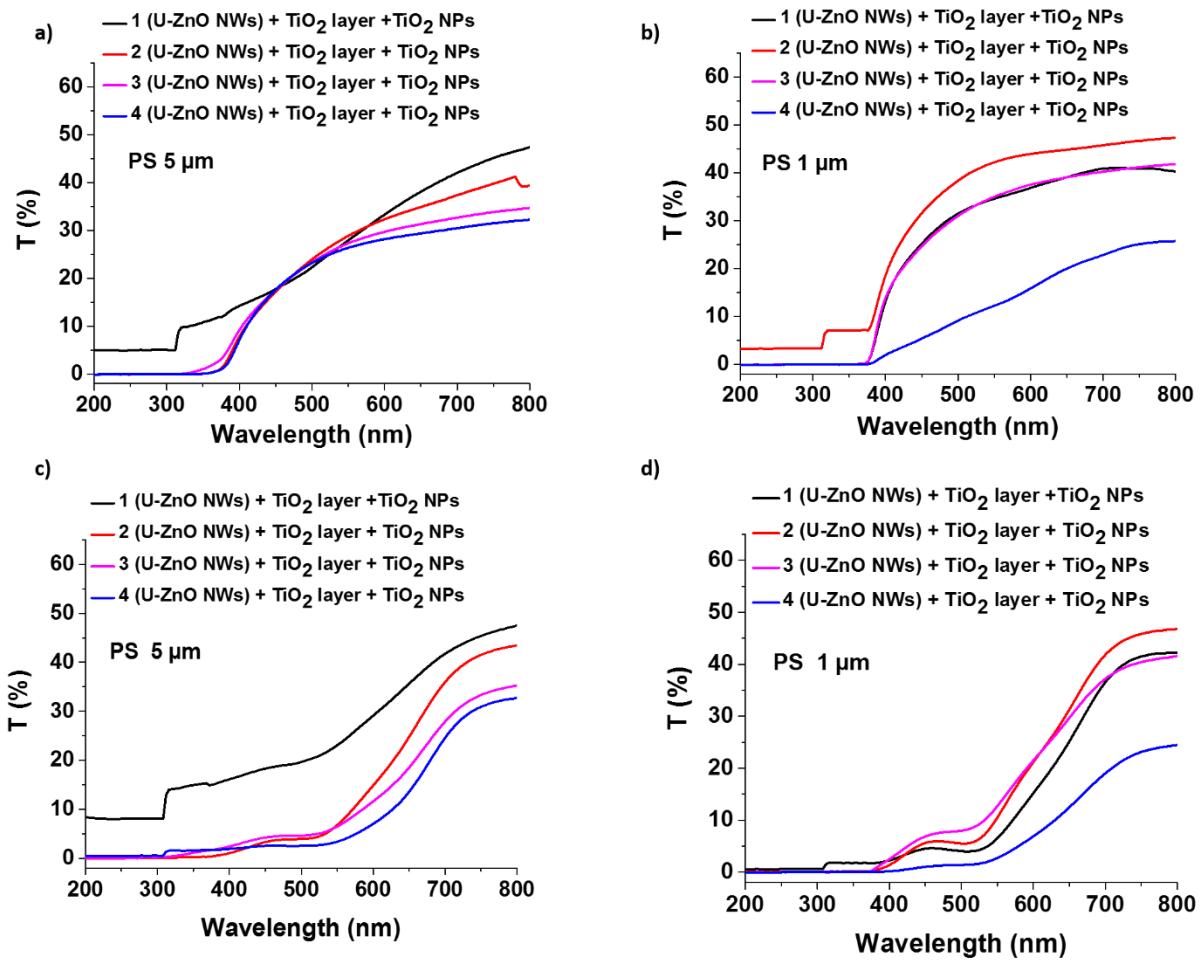

Figure 5. Transmittance spectra of the DSSCs based on multilayers of U-ZnO NWs/ $TiO_{2\ 10nm}$/ $TiO_{2\ NPs}$ cells before dye loading (a, b) and after dye loading and illumination (c, d).

The absorbance of the U-ZnO NWs/$TiO_{2\ 10nm}$/$TiO_{2\ NPs}$ cell was analyzed before (Figure S7a, b), and after dye loading and illumination (Figure S7c, d) to determine the influence of the U-ZnO NW multilayers combined with the mesoporous film (~ 10 µm) of TiO_2 NPs. For the U-ZnO NWs/$TiO_{2\ 10nm}$/$TiO_{2\ NPs}$ samples, the absorbance increased from 87% for a monolayer of urchins to 97% when depositing four layers of U-ZnO NWs (~ 5µm-PS) which shows an enhancement in the light scattering caused by the higher surface of the multilayers (four layers) based U-ZnO NWs (Figure S7a). As explained from the transmittance feature, the TiO_2

mesoporous film also contributed to increasing the absorption proportionally to the number of PS layers. Similarly, in samples with 1µm-PS, the absorbance showed an increase to about ~ 97% of incident light for the multilayers, despite their spatial inhomogeneity.

The absorbance was boosted, in the range of ~ 200 nm and ~ 650 nm, after dye addition and illumination. This increase was caused by the huge amount of dye contained in the thick top layer of TiO_2 NPs (10 µm) (Figure S7c and d) [19, 36].

3. Performance of the hybrid nanoparticle core-shell structure as a solar cell

In principle, the resulting solar cell based on multilayers of U-ZnO NWs coated with TiO_2 NPs could be directly used in DSSCs adopting the "back-side" illumination configuration. Nevertheless, "front-side" illumination was used to obtain higher cell efficiencies compared with the backside configuration. Specifically, the photo-anode was on the front-side and was irradiated through the ITO-coated glass to minimize light losses due to light absorption in the electrolyte and in the platinum coating of the counter electrode [37]. For the performance analysis, results obtained with the experimental solar cells were compared with those obtained using a reference DSSC made of a 10 µm mesoporous film of TiO_2 NPs using the same fabrication method as for the U-ZnO NWs/$TiO_{2\ 10nm}$/$TiO_{2\ NPs}$.

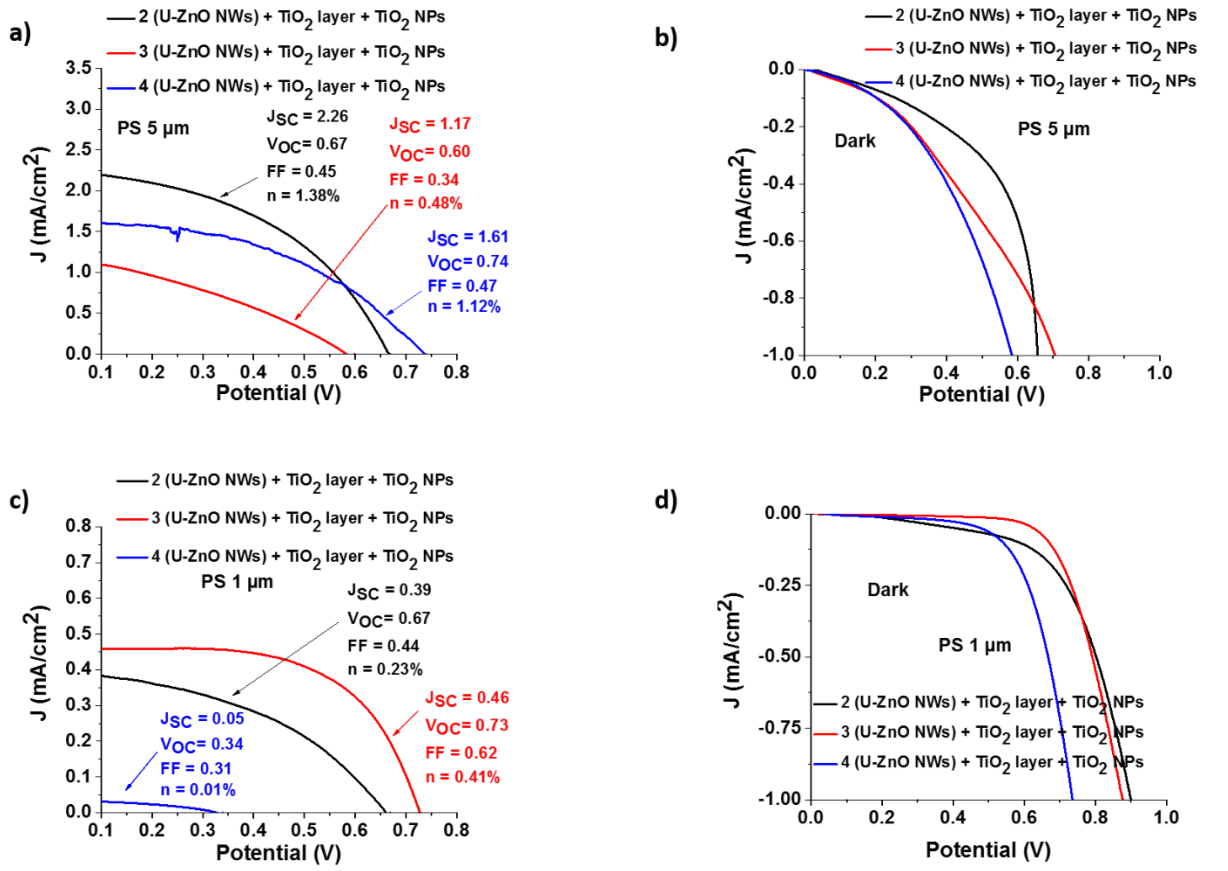

Figure 6. *J-V* data for DSSCs based on multilayers of U-ZnO NWs covered with a 10nm-thick layer of TiO_2 (ALD) with on top TiO_2 NPs. Each cell was sensitized in dye solution for 12h. Power plots **(a) (c)** under **500 Wm^{-2}** simulated sunlight, and **(b) (d)** in the dark**.** The short-circuit current density (J_{sc}), the open-circuit voltage (V_{oc}), the fill factor (FF) and the overall photoconversion efficiency (µ (%)) are specified for each device.

The open-circuit voltage (V_{oc}) of solar cells based on U-ZnO NWs/$TiO_{2\ 10nm}$/$TiO_{2\ NPs}$ increased with four U-ZnO NWs layers (5µm-PS) compared with samples with only a monolayer of urchins [19] (Table 3). This was probably explained by the significant increase of the surface area, due to the additional layers, and the consequent increase of dye loading. However, cell efficiency decreased from 1.8% for a monolayer to 1.38% and 0.48% when assembling two

layers and three layers of U-ZnO NWs, respectively, and to 1.12% for four layers (Table 3). The J_{SC} decreased from 2.64 mA/cm^2 for monolayer to 2.26 mA/cm^2 and 1.17 mA/cm^2 for two- and three-layer U-ZnO NWs, respectively, and to 1.61 mA/cm^2 for four layers of urchins (Table 3). The FF decreased from 0.5 for a monolayer to 0.45 and 0.34 for two layers and three layers of U-ZnO NWs, respectively (Figure 6a, black and red curve, respectively, and Table 3), and to 0.47 in the case of four layers of urchins (PS 5 µm) (Figure 6a, b, blue curve, and Table 3). The decrease of these parameters can be explained by the fact that adding more layers of urchins increases the distance travelled by the electrons, and consequently also the recombination of charges, as observed from the high dark currents (Figure 6 and Table 3). In summary, for cells based on 5µm-PS, the best J_{SC} and efficiency values were obtained for two-layer of U-ZnO NWs (2.26 mA cm^{-2} and 1.38%, respectively) compared with three-layer (1.17 mA cm^{-2} and 0.48%, respectively) and four-layer U-ZnO NWs (1.61 mA cm^{-2} and 1.12%, respectively). In our case, the bilayer structure provided the optimal travelling distance for electrons.

Analysis of the same parameters in solar cells based on U-ZnO NWs/$TiO_{2\ 10nm}$/TiO_2 NPs (1µm-PS) showed that DSSCs displayed deficient transportation and low efficiency (highest conversion efficiency: 0.41% for DSSCs based on three layers of U-ZnO NWs with 1µm-PS) (Table 3). Several factors could explain these findings: i) the higher surface area for 1µm-PS could be unfavorable for the collection process because it can increase the recombination centers through the structure; ii) a poor morphological effect, possibly caused by the fact that the 1µm-PS barely contacting each other, could force the electrons to flow through narrow channels, thus decreasing their characteristic diffusion lengths and reducing the electrical conductivity in the structure. Thus, urchins based on 5 µm-PS allowed a better performance of the solar cell (see Table 3).

Efficiency is a compromise between the effective photon absorption and charge carriers collection. These results prove that an optimal number of layers is needed to provide a higher surface area without hindering the travelling distance of electrons. As the absorbance of U-ZnO NW layers was high enough (>90% for all numbers of layers) to neglect its negative impact on efficiency, the electron transportation inadequacy remains the most probable reason for this low efficiency. The highly activated surface area provided by the 3D multilayers of U-ZnO NWs could be an interesting architecture for gas- and UV-sensing devices [38] because the physical interactions are mostly manifested on the surface.

Table 3. V_{OC}, FF, J_{SC} and efficiency in function of the number of U-ZnO NWs layers and the PS size in the presence of a TiO_2 layer and TiO_2 NPs.

Samples (U-ZnO NWs/ TiO_2 ALD $_{10\ nm}$/ TiO_2 NPs)	**V_{OC} (V)**	**FF (mV)**	**J_{SC} (mA cm^{-2})**	**Efficiency (%)**
1 layer U-ZnO NWs (5µm-PS) [19]	0.68	0.5	2.64	**1.8**
1 layer U-ZnO NWs (1µm-PS)	0.54	0.33	0.11	**0.04**
2 layers U-ZnO NWs (5µm-PS)	0.67	0.45	2.26	**1.38**
2 layers U-ZnO NWs (1µm-PS)	0.67	0.44	0.39	**0.23**
3 layers U-ZnO NWs (5µm-PS)	0.60	0.34	1.17	**0.48**
3 layers U-ZnO NWs (1µm-PS)	0.73	0.62	0.46	**0.41**

4 layers U-ZnO NWs (5µm-PS)	0.74	0.47	1.61	**1.12**
4 layers U-ZnO NWs (1µm-PS)	0.34	0.31	0.05	**0.01**
Reference DSSC: TiO_2 NPs (10 µm**)**	0.64	0.59	2.03	**1.5**

4. Discussion

The best J_{SC} values and photovoltaic efficiencies (2.64 mA cm^{-2} and 1.8%, respectively) were obtained for monolayers of urchins (5µm-PS). This result can be explained by the shorter distance traveled by electrons through the urchin monolayer to reach the electrode. The TiO_2 NPs used as reference DSSC had a conversion efficiency of 1.5% (Table 3). This lower efficiency compared with literature data [39] could be explained mainly by the charge carrier recombination at the NPs contact points, but also by our "homemade" lighting system. Nevertheless, this highlights the high potential of multilayer U-ZnO NWs as conductive nanoscaffolds.

Among the multilayers of urchins, the best J_{SC} values and photovoltaic efficiencies were obtained for U-ZnO NWs based on bilayers of urchins and PS spheres with a diameter of 5 µm (2.26 mA cm^{-2} and 1.38%; Table 3). Bilayers of urchins (5µm-PS) might represent the optimum number of layers to provide a larger active surface area and minimize the charge transfer problem.

Despite the fact that the efficiency of our DSSC cells (1.38%) based on bilayers was lower than that of cells based on monolayers of urchins (1.8%) [19], the overall conversion efficiency increased compared with the efficiency of ZnO NWs (0.8% and 0.7% [16, 40, 41]), ZnO NPs (0.65) [42, 43] and ZnO nanotubes (0.29%) [44]. Our objective was not to obtain the highest efficiency, but to

compare the ZnO NWs and U-ZnO NWs structures as well as the effect of the number of urchin layers on the performance of the DSSC.

As previously reported[45], choosing the right diameter of structures is the key factor for improving the overall DSSC efficiency.

Finding reports in the literature that compare the number of layers of ZnO nanostructures is not straightforward because this architecture is a novel strategy to increase the surface area. Some researchers reported that the use of multilayers results in an increase of the overall conversion efficiency [46-48]. However, in our case, adding more layers of urchins was detrimental for the DSSC efficiency, despite the increase of dye loading and light absorption. This could be attributed to the poor electrical connection among multilayers of urchins, and to the possible formation of dye aggregates. Therefore, we think that further optimization of the urchin fabrication process will increase the PCE.

Adding TiO_2 NPs on top of the ZnO/TiO_2 core-shell enhanced the characteristic parameters of the solar cell by reducing the charge recombination. Although, the dye solution could be chemisorbed on the TiO_2 NPs present on the inner surface of the urchins (Figure S10 in Supporting Information), the dye is expected to be adsorbed mainly on the NWs that are outside of the pores. Therefore, extensive work will focus on improving the surface area and reducing the urchin hole area.

Although the performance of our DSSC cells was lower than that obtained with standard NP-based solar cells, their efficiency can be improved by depositing a film of perovskite absorber as light-harvesting active layer [35, 49].

CONCLUSION

In this study we describe the design and characterization of multilayers of urchin-like ZnO NWs coated with TiO_2 nanostructures and used as photo-anode in dye-sensitized solar cells. A low cost-deposition technique with an ALD reactor was used to grow these multilayers of U-ZnO NWs using two PS size (5 µm and 1 µm in diameter). The resulting multilayer U-ZnO NWs were coated with a 10nm-thick amorphous TiO_2 shell by ALD, followed by annealing at 450 °C to obtain the anatase phase. After the deposition of TiO_2 NPs to further increase the surface area, these core-shell nanostructures were sensitized with a solution of Ru dye (N719).

By increasing the number of layers, the photon absorption increased compared with that of a monolayer of U-ZnO NWs. Conversely, the photovoltaic efficiency decreased due to the charge recombination because of the long distance travelled by electrons through the structure. Therefore, the monolayer of urchins showed the highest efficiency. Among the devices based on multilayers of urchins, the solar cell based on bilayer U-ZnO NWs (5µm-PS) showed a good performance due to the compromise between high surface area and distance traveled by electrons. Conversely, solar cells based on urchins with 1µm-PS displayed higher photon absorption and lower efficiency compared with DSSCs based on 5µm-PS. This is probably explained by the low electrical connection between the urchin layers. Finally, the photogenerated current was transported through the multilayer U-ZnO NWs, highlighting the high conductivity of these core-shell nanostructures. Further optimization could improve the overall photoconversion efficiency.

SUPPORTING INFORMATION

Figure S1: SEM images of the multilayers based on U-ZnO NWs; Figure S2: SEM images of different sizes of PS spheres used for the synthesis of the multilayers based U-ZnO NWs; Figure

S3: X-Ray Diffraction (XRD) peaks of U-ZnO NWs multilayers; Figure S4: Absorbance spectra of **a)** multilayers U-ZnO NWs (PS ~ 5 µm) and **b)** multilayers U-ZnO NWs (PS ~ 1 µm); Figure S5: Reflection spectra of a) multilayers U-ZnO NWs (PS ~ 5 µm) and b) multilayers U-ZnO NWs (PS ~ 1 µm); Figure S6: SEM images of multilayers urchin-like ZnO-TiO_2 core-shell and TiO_2 nanoparticle ensemble; Figure S7: Absorbance spectra of the DSSC based on multilayers of U-ZnO $_{NWs}$ / $TiO_{2\ 10\ nm\ layer}$ / $TiO_{2\ NPs}$ before (a), (b) and (c), (d) after illumination; Figure S8: Reflection spectra of the DSSC based on multilayers of U-ZnO $_{NWs}$ / $TiO_{2\ 10\ nm\ layer}$ / $TiO_{2\ NPs}$ after illumination; Figure S9: Cross-sectional SEM image of individual hollow U-ZnO NWs grown on the PS spheres covered with 20 nm of ZnO ALD layer, after plasma etching treatment of 25 min; Figure S10: Cross-sectional SEM images showing a bilayer urchin-like ZnO-TiO_2 core-shell coated with 10 nm of anatase TiO_2 and TiO_2 NP material; Table S1: Volume of TiO_2 without considering the porosity and without subtracting U-ZnO NWs volumes; Table S2: Volume of U-ZnO NWs for different substrate surface (gaskets); Table S3: Volume of TiO_2 without considering the porosity; Table S4: Volume of TiO2 with porosity (33%); Table S5: Volume of pores; Table S6: Number of TiO_2 nanoparticles taking into account the porosity (33%); Table S7: Surface of TiO_2 nanoparticles; Table S8: Active surface area of U-ZnO NWs (PS 5 µm or PS 1 µm and different sizes of substrates); Table S9: Total active surface area of the samples.

ACKNOWLEDGMENTS

The joint funding program between the Lebanese National Council for Scientific Research CNRS-L and the University of Montpellier UM supported Chantal Karam's PhD project. The authors would like to thank Mr. Edy AZRAK for the SEM-FIB manipulation and for the TEM

characterization of the obtained materials. The authors would like to thank also Dr. Ivo Utke and Mr. Carlos Guerra-Nuñezc from EMPA (Switzerland) for DSSC fabrication and measurement.

REFERENCES

1. Beard, M.C.; Luther J.M.; Nozik A.J. The Promise and Challenge of Nanostructured Solar Cells. Nat. Nanotechnol., **2014**, 9, 951-4.
2. Guerra-Nuñez, C.; Park H.G.; Utke I. In *Atomic Layer Deposition in Energy Conversion Applications*; Bachmann, J., Ed.; Wiley-VCH Verlag GmbH & Co. KGaA., **2017**, Chapter 4, 119-148.
3. Kang Xiaohui, J.C.; Wan Z.; Zhuang J.; Feng, J.; A Novel Tri-Layered Photoanode of Hierarchical ZnO Microspheres on 1D ZnO Nanowire Arrays for Dye-Sensitized Solar Cells. RSC Adv., **2015**, 5, 16678-16683.
4. Suhaimi, S.; Mukhzeer, M.; Alahmed, Z.A.; Chyský, J.; Reshak, A.H.; Materials for Enhanced Dye-Sensitized Solar Cell Performance: Electrochemical Application. Int. J. Electrochem. Sci., **2015**, 10, 2859-2871.
5. Benkstein, K. D.; Kopidakis, N.; Van de Lagemaat J.; Frank A. J. Influence of the Percolation Network Geometry on Electron Transport in Dye-Sensitized Titanium Dioxide Solar Cells. J. Phys. Chem. B, **2003**, 107, 7759-7767.
6. Li, Q.; Yun, F.; Li, Y.; Ding, W.; Zhang, Y. Fabrication and Application of Indium-Tin-Oxide Nanowire Networks by Polystyrene-Assisted Growth. Scientific Reports, **2017**, 7, 1600.
7. Parize, R.; Katerski, A.; Gromyko, I.; Rapenne, L.; Roussel, H.; Kärber, E.; Appert, E.; Krunks, M.; Consonni, V.; ZnO/TiO2/Sb2S3 Core–Shell Nanowire Heterostructure for Extremely Thin Absorber Solar Cells. J. Phys. Chem. C, **2017**, 121, 9672-9680.
8. Zhang, A.; Zheng, G.; Lieber, C. In *Nanowires*; Zhang, A.; Zheng, G.; Lieber, C., Eds.; Springer, **2016**, Chapter 1, 1-13.
9. Zhou, X.; Zhang, Q.i.; Gan, L.; Li, X.; Li, H.; Zhang, Y.; Golberg, D.; Zhai, T. High Performance Solar-Blind Deep Ultraviolet Photodetector Based on Individual Single-Crystalline Zn2GeO4 Nanowire. Adv. Funct. Mater, **2016**, 26, 704-712.
10. Yan, R.; Gargas, D.; Yang, P.; Nanowire Photonics. Nat. photonics, **2009**, 3, 569-576.
11. Knez, M.; Scholz, R.; Nielsch, K.; Pippel, E.; Hesse, D.; Zacharias, M.; Gösele, U. Monocrystalline Spinel Nanotube Fabrication Based on The Kirkendall Effect. Nat. Mater., **2006**, 5, 627-631.
12. Elias, J.; Lévy-Clément, C.; Bechelany, M.; Michler, J.; Wang, G.Y.; Wang, Z.; Philippe, L. Hollow Urchin-Like ZnO Thin Films by Electrochemical Deposition. Adv. Mater., **2010**, 22, 1607–1612.
13. Elias, J.; Bechelany, M.; Utke, I.; Erni, R.; Hosseini, D.; Michler, J.; Philippe, L. Urchin-Inspired Zinc Oxide as Building Blocks for Nanostructured Solar Cells. Nano Energy, **2012**, 1, 696-705.
14. Law, M.; Greene, L. E.; Radenovic, A.; Kuykendall, T.; Liphardt, J.; Yang, P. ZnO− Al2O3 and ZnO− TiO2 Core− Shell Nanowire Dye-Sensitized Solar Cells. J. Phys. Chem. B, **2006**, 110, 22652-22663.
15. Baxter, J.B.; Aydil, E.S. Nanowire-Based Dye-Sensitized Solar Cells. Appl. Phys. Lett., **2005**, 86, 053114.
16. Guillen, E.; Azaceta, E.; Laurence, M.P; Zukal, A.; Tena-Zaera, R.; Anta, J. A. ZnO Solar Cells With An Indoline Sensitizer: A Comparison Between Nanoparticulate Films and Electrodeposited Nanowire Arrays. Energy Environ. Sci., **2011**, 4, 3400-3407.
17. Law, M.; Greene, L.E.; Johnson, J. C.; Saykally, R.; Yang, P. Nanowire Dye-Sensitized Solar Cells. Nat. Mater., **2005**, 4, 455–459.

18. Elias J.; Utke, I.; Yoon S.; Bechelany M.; Weidenkaff A.; Michler J.; Philippe L. Electrochemical Growth of ZnO Nanowires on Atomic Layer Deposition Coated Polystyrene Sphere Templates. Electrochim. Acta, **2013,** 110, 387-392.
19. Karam C.; Guerra-Nuñez, C.; Habchi R.; Herro Z.; Abboud N.; Khoury A.; Tingry S.; Miele P.; Utke I.; Bechelany M. Urchin-Inspired ZnO-TiO2 Core-Shell as Building Blocks for Dye Sensitized Solar Cells. Mater. Des., **2017**, 126, 314-321.
20. Marichy, C.; Bechelany, M.; Pinna, N.; Atomic Layer Deposition of Nanostructured Materials for Energy and Environmental Applications. Adv. Mater., **2012**, 24, 1017-1032.
21. Cao, B.; Li, Y.; Duan, G.; Cai, W. Growth of ZnO Nanoneedle Arrays with Strong Ultraviolet Emissions by an Electrochemical Deposition Method. Cryst. Growth Des., **2006,** 6, 1091-1095.
22. Cho, A.Y.; Arthur, J.R. Molecular Beam Epitaxy. Prog. solid state chem., **1975,** 10, 157-191.
23. Liu, X.; Wu, X.; Cao, H.; Chang, R. P. H. Growth Mechanism and Properties of ZnO Nanorods Synthesized by Plasma-Enhanced Chemical Vapor Deposition. J. Appl. Phys., **2004,** 95, 3141-3147.
24. Tigli, O.; Juhala, J. ZnO Nanowire Growth by Physical Vapor Deposition. *11th IEEE International Conference on Nanotechnology*. **2011**.
25. Miki, F.; Noriaki, K.; Masanori S.; Yoshiji, H. Molecular Beam Epitaxy Growth of ZnO Using Initial Zn Layer and MgO Buffer Layer on Si (111) Substrates. J. Vac. Sci. Technol., B: Microelectron. Nanometer Struct.Process., Meas., Phenom., **2004**. 22, 1484-1486.
26. Zhang, Y.; Guerra-Nuñez, C.; Utke, I.; Michler, J.; Rossell, M.D; Erni, R. Understanding and Controlling Nucleation and Growth of TiO2 Deposited on Multiwalled Carbon Nanotubes by Atomic Layer Deposition. J. Phys. Chem. C, **2015**, 119, 3379-3387.
27. Guerra-Nuñez, C.; Zhang, Y.; Li, M.; Chawla, V.; Erni, R.; Michler, J.; Gyu Park, H.; Utke, I. Morphology and Crystallinity Control of Ultrathin TiO Layers Deposited on Carbon Nanotubes by Temperature-Step Atomic Layer Deposition. Nanoscale, **2015,** 7, 10622-10633.
28. Cabello-Aguilar, S.; Balme, S.; Abou Chaaya, A.; Bechelany, M.; Balanzat, E.; Janot, J.M.; Pochat-Bohatier, C.; Miele, P.; Dejardin, P. Slow Translocation of Polynucleotides and Their Discrimination by Alpha-Hemolysin Inside a Single Track-Etched Nanopore Designed by Atomic Layer Deposition. Nanoscale, **2013,** 5, 9582-9586.
29. Abou Chaaya, A.; Le Poitevin, M.; Cabello-Aguilar, S.; Balme, S.; Bechelany, M.; Kraszewski, S.; Picaud, F.; Cambedouzou, J.; Balanzat, E.; Janot, J.M.; Thami, T.; Miele,P.; Dejardin, P. Enhanced Ionic Transport Mechanism by Gramicidin A Confined Inside Nanopores Tuned by Atomic Layer Deposition. J. Phys. Chem. C, **2013,** 117, 15306-15315.
30. Viter, R; Abou Chaaya, A.; Iatsunskyi, I.; Nowaczyk,G.; Kovalevskis, K.; Erts, D.; Miele, P.; Smyntyna, V.; Bechelany, M. Tuning of ZnO 1D Nanostructures by Atomic Layer Deposition and Electrospinning for Optical Gas Sensor Applications. Nanotechnology, **2015,** 26, 105501.
31. Baitimirova, M.; Viter, R.; Andzane, J.; Van der Lee, A.; Voiry, D.; Iatsunskyi, I.; Emerson, C.L.; Mikoliunaite, L.; Tumenas, S.; Za##ski, K.; Balevicius, Z.; Baleviciute, L.; Ramanaviciene, A.; Ramanavicius, A.; S.; Erts, D.; Bechelany, M. Tuning of Structural and Optical Properties of Graphene/ZnO Nanolaminates. J. Phys. Chem. C, **2016,** 120, 23716-23725.
32. Donovan, M.; Benjamin, B., Roche, J. Efficiency VS. Irradiance Characterization of PV Modules Requires Angle-of-Incidence and Spectral Corrections. *35th IEEE Photovoltaic Specialists Conference*. **2010**.
33. Guillemin, S.; Rapenne, L.; Roussel, H.; Sarigiannidou, E.; Brémond, G.; Consonni, V. Formation Mechanisms of ZnO Nanowires: The Crucial Role of Crystal Orientation and Polarity. J. Phys. Chem. C, **2013**, 117, 20738-20745.
34. Ghann, W.; Rahman, A.; Rahman, A.; Uddin, J. Interaction of Sensitizing Dyes with Nanostructured TiO2 Film in Dye-Sensitized Solar Cells Using Terahertz Spectroscopy. Sci. Rep., **2016**, 6, 30140.

35. Liu, M.; Johnston, M.B.; Snaith, H.J. Efficient Planar Heterojunction Perovskite Solar Cells by Vapour Deposition. Nature, **2013**, 501, 395-398.
36. Luping, L.; Cheng, X.; Yang, Z.; Shikai, C.; Kirk, Z. Improving Performance via Blocking Layers in Dye-Sensitized Solar Cells Based on Nanowire Photoanodes. ACS Appl. Mater. Interfaces, **2015**, 7, 12824-12831.
37. Mohammad, F.; Moradi, M.; Lee, K.; Cha, G.; So, S.; Kahnt, A.; Guldi, D. M.; Altomare, M.; Schmuki, P.; Enhanced Performance of Dye-Sensitized Solar Cells Based on TiO2 Nanotube Membranes Using an Optimized Annealing Profile. Chem. Commun., **2015**, 51, 1631-1634.
38. Makhlouf, H.; Karam, C.; Lamouchi, A.; Tingry, S.; Miele, P.; Habchi, R.; Chtourou, R.; Bechelany, M.; Analysis of Ultraviolet Photo-Response of ZnO Nanostructures Prepared by Electrodeposition and Atomic Layer Deposition. Appl. Surf. Sci., **2018**, 444, 253-259.
39. Mojaddami, M.; Andaji Garmaroudi, Z.; Mohammadi, M. R.; Madaah Hosseini, H. R.; Efficient Dye-Sensitized Solar Cells Based on TiO2 Nanoparticles and Skein-Like Nanotubes: Effect of Arrangement Modes of the Layers and TiCl4 Treatment. J. Taiwan Inst. Chem. Eng., **2016**, 61, 138-146.
40. Marimuthu T.; Anandhan, N.; Thangamuthu, R.; Mummoorthi, M.; Ravi, G.; Synthesis of ZnO Nanowire Arrays on ZnOTiO2 Mixed Oxide Seed Layer for Dye Sensitized Solar Cell Applications. J. Alloys Compd., **2016**, 677, 211-218.
41. Junjie, Q.; Liu, W.; Biswas, C.; Zhang, G.; Sun, L.; Wang, Z.; Hu, X.; Zhang, Y.; Enhanced Power Conversion Efficiency of CdS Quantum Dot Sensitized Solar Cells with ZnO Nanowire Arrays as the Photoanodes. Opt. Commun, **2015**, 349, 198-202.
42. Choudhury, M.S.H.; Kishi, N.; Soga, T.; Compression of ZnO Nanoparticle Films at Elevated Temperature for Flexible Dye-Sensitized Solar Cells. J. Alloys Compd, **2016**, 656, 476-480.
43. Sobuś, J.; Burdzinski, G.; Karolczak, J.; Idígoras, J.; Anta, J.A.; Ziółek, M.; Comparison of TiO2 and ZnO Solar Cells Sensitized with an Indoline Dye: Time-Resolved Laser Spectroscopy Studies of Partial Charge Separation Processes. Langmuir, **2014**, 30, 2505-2512.
44. Rahman, M. Y. A.; Roza, L.; Umar, A. A.; Salleh, M. M.; Effect of Boric Acid Composition on the Properties of ZnO Thin Film Nanotubes and the Performance of Dye-Sensitized Solar Cell (DSSC). J. Alloys Compd, **2015**, 648, 86-91.
45. Pfau, M.W.; Kunzmann, A.; Segets, D.; Peukert, W.; Wallace, G.G.; Officer, D.L.; Clark, T.; Costa, R.D., Guldi, D.M., Choosing the Right Nanoparticle Size - Designing Novel ZnO Electrode Architectures for Efficient Dye-Sensitized Solar Cells. J. Mater. Chem. A, **2017**, 5, 7516-7522.
46. Hejazi, S.M.H.; Mohandesi, J.A.; Javanbakht, M.; The Effect of Functionally Graded Porous Nano Structure TiO2 Photoanode on Efficiency of Dye Sensitized Solar Cells. Sol. Energy, **2017**, 144, 699-706.
47. Xu, C.; Wu, J.; Desai, U.V.; Gao, D.; Multilayer Assembly of Nanowire Arrays for Dye-Sensitized Solar Cells. J. Am. Chem. Soc., **2011**, 133, 8122-8125.
48. Guldin, S.; Hüttner, S.; Kolle, M.; Welland, M.E.; Müller-Buschbaum, P.; Friend, R.H.; Steiner, U.; Tétreault, N.; Dye-Sensitized Solar Cell Based on a Three-Dimensional Photonic Crystal. Nano Lett., **2010**, 10, 2303-2309.
49. Ball, J.M.; Lee, M.M.; Hey, A.; Snaith, H.J.; Low-Temperature Processed Meso-Superstructured to Thin-Film Perovskite Solar Cells. Energy Environ. Sci. **2013**, 6, 1739-1743.

GRAPHICAL ABSTRACT

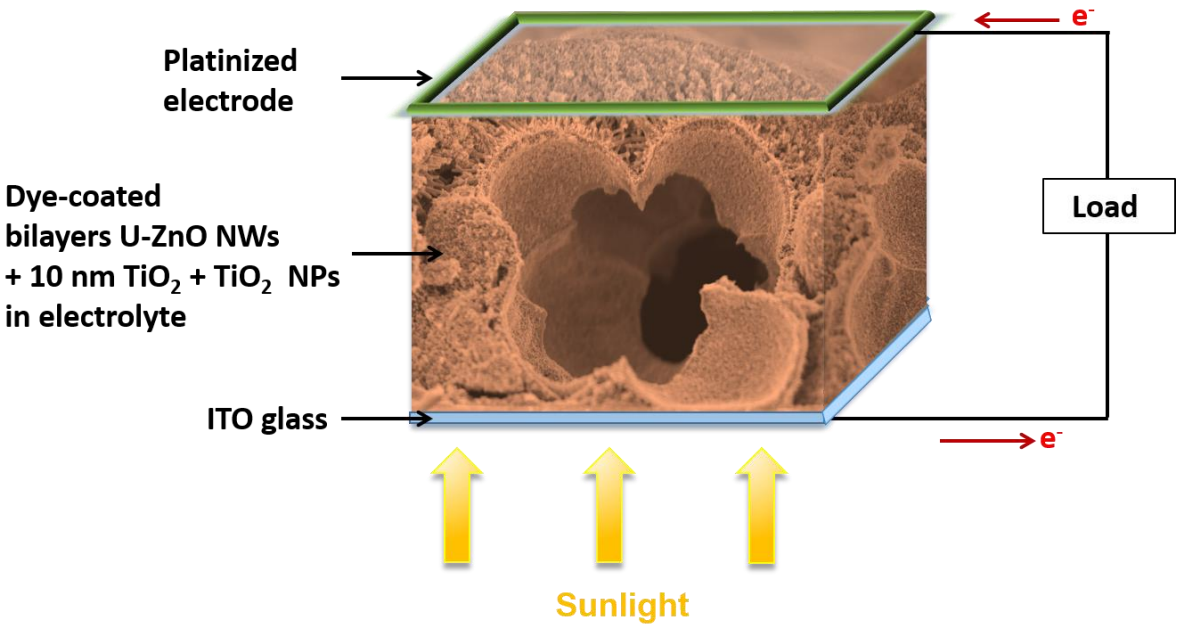
Platinized
electrode
Dye-coated
bilayers U-ZnO NWs
+ 10 nm TiO_2 + TiO_2 NPs
in electrolyte
ITO glass
e-
Load
e-
Sunlight